The effect of H- and J-aggregation on the photophysical and photovoltaic properties of small Thiophene–Pyridine–DPP molecules for bulk-heterojunction solar cells

Document Version:
Publisher's PDF, also known as Version of Record (includes final page, issue and volume numbers)

Please check the document version of this publication:

• A submitted manuscript is the version of the article upon submission and before peer-review. There can be important differences between the submitted version and the official published version of record. People interested in the research are advised to contact the author for the final version of the publication, or visit the DOI to the publisher's website.
• The final author version and the galley proof are versions of the publication after peer review.
• The final published version features the final layout of the paper including the volume, issue and page numbers.
Link to publication

FULL PAPER

The Effect of H- and J-Aggregation on the Photophysical and Photovoltaic Properties of Small Thiophene–Pyridine–DPP Molecules for Bulk-Heterojunction Solar Cells

Miriam Más-Montoya and René A. J. Janssen*

The performance of organic semiconductors in optoelectronic devices depends on the functional properties of the individual molecules and their mutual orientations when they are in the solid state. The effect of H- and J-aggregation on the photophysical properties and photovoltaic behavior of four electronically identical but structurally different thiophene–pyridine–diketopyrrolopyrrole molecules is studied. By introducing and changing the position of two hexyl side chains on the two peripheral thiophene units of these molecules, their aggregation in thin films between H-type and J-type is effectively tuned, as evidenced from the characteristics of optical absorption, fluorescence, and excited state lifetime. The two derivatives that assemble into J-type aggregates exhibit a significantly enhanced photovoltaic performance, up to an order of magnitude, compared to the two molecules that form H-type aggregates. The reasons for this remarkably different behavior are discussed.

1. Introduction

The progress of organic photovoltaic technology has been closely related to the development of new organic materials with excellent semiconducting properties and optical absorption. After a decade of intense research, chemists and material scientists have designed many original building blocks and have developed elegant novel strategies to combine different units, creating highly efficient materials, both small molecules and polymers, exhibiting the desired properties for photovoltaic applications.[1] In comparison with polymers, the interest for small-molecule materials is motivated by their more easy purification and characterization, the well-defined molecular

structure, and the perfectly reproducible synthetic procedures that largely avoid the variability between different batches seen in polymerizations. Recently, successful small-molecule donor systems have been reported that reach high power conversion efficiencies (PCEs) in organic solar cells.[2] The combination of a judicious molecular design with the optimal material processing conditions and device engineering remains a critical point for the success in the photoenergy conversion process. Rational molecular design is of great importance for further improving the photovoltaic performance of small-molecule bulk-heterojunction organic solar cells. However, achieving a high performance employing newly designed small-molecule materials remains a challenge because it is difficult to predict in sufficient detail how molecules assemble in thin films and how this affects photovoltaic performance.

When small-molecule chromophores assemble in the solid state, they often form H-type or J-type aggregates, depending on the relative alignment of the transition dipole moments on adjacent molecules. In an H-aggregate, molecules stack predominantly face-to-face, while J-aggregates form when molecules primarily stack in a head-to-tail arrangement. The formation of such aggregates has important consequences for the energies of the excited states and the oscillator strengths of the transitions to these states from the ground state. Consequently, H- and J-aggregation can strongly modify optical absorption and the photoluminescence spectra. To contribute to our understanding of the effect of molecular packing on photovoltaic performance, it is of interest to assemble one type of molecule in different packing modes.

In this contribution, we do that by using molecules based on diketopyrrolopyrrole (DPP) flanked by two 5-(thiophen-2-yl)pyridin-2-yl units in which solubilizing hexyl side chains are introduced on the free positions of the peripheral thiophene units (**Scheme 1**). The DPP fragment has been extensively explored for organic semiconductors, because of its strong optical absorption and excellent charge transport properties,[3] especially for the design of materials for organic photovoltaic applications.[4] The electron density of the DPP core can be modified by employing different (hetero)aromatic flanking groups. The combination of DPP with two flanking pyridin-2-yl moieties leads to the simultaneous decrease of the frontier energy levels due to the electron-withdrawing nature of

Dr. M. Más-Montoya, Prof. R. A. J. Janssen
Molecular Materials and Nanosystems
Institute for Complex Molecular Systems
Eindhoven University of Technology
P.O. Box 513, 5600 MB, Eindhoven, The Netherlands
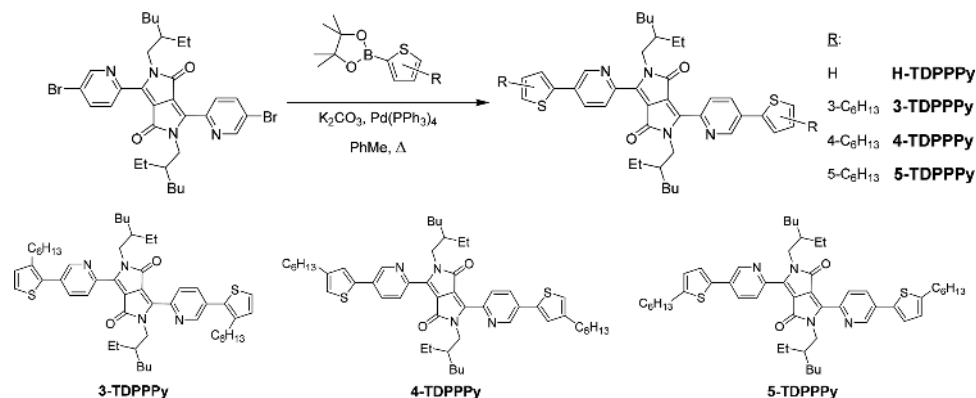E-mail: r.a.j.janssen@tue.nl
Prof. R. A. J. Janssen
Dutch Institute for Fundamental Energy Research
De Zaale 20, 5612 AJ, Eindhoven, The Netherlands

ADVANCED
FUNCTIONAL
MATERIALS
www.afm-journal.de

ADVANCED
SCIENCE NEWS
www.advancedsciencenews.com

FULL PAPER

Scheme 1. Synthetic pathway of the thiophene end-capped pyridine–DPP derivatives and structures of the synthesized compounds bearing an alkyl chain at different positions in the thiophene ring.

the pyridine ring, enhancing the chances for a high open-circuit voltage in an organic solar cell.[5] This feature makes the pyridine-flanked DPP fragment an interesting building block for organic photovoltaics. Although their potential has been explored much less than for thiophene-flanked DPP derivatives, the power conversion efficiencies reached in polymer solar cells with pyridine-flanked DPP are similar to those of thiophene-flanked DPP polymers.[6] DFT calculations have shown that the reduced steric hindrance of the nitrogen atom in the 1-position of the pyridin-2-yl rings with the alkyl substituents on the DPP core, as compared to phenyl, effectively reduces the dihedral angle to a fully coplanar geometry that maximizes the possibility for intermolecular π–π interactions.[5m]

The position,[7] length,[8] and stereoisomerism[9] of the aliphatic chains attached to the aromatic backbone of the semiconductor small molecules is known to affect the morphology in the solid state, and thereby the optoelectronic properties and the photovoltaic performance. By introducing hexyl side chains on different positions of the terminal thiophene rings, we find that it is possible to effectively tune the packing in thin films between H-like and J-like aggregates. The H-type and J-type aggregates exhibit distinctly different photophysical properties in absorption, fluorescence, and excited state lifetime. Remarkably, we find that the two derivatives that assemble into J-type aggregates exhibit a significantly enhanced photovoltaic performance compared to the two molecules that form H-type aggregates. The difference in PCE is up to an order of magnitude. We study charge generation, charge recombination, and charge transport to obtain a deeper insight in the causes of the behavior and how subtle structural changes induce large effects in the properties of small-molecule donor materials.

2. Results and Discussion

2.1. Synthesis

The synthetic route for the four pyridine–DPP derivatives is outlined in Scheme 1. 3,6-Bis(5-bromopyridin-2-yl)-2,5-bis(2-ethylhexyl)-2,5-dihydropyrrolo[3,4-c]pyrrole-1,4-dione was synthesized according to a previously reported procedure,[5n] using a traditional pseudo-Stobbe condensation reaction

between 5-bromo-2-pyridinecarbonitrile and diethyl succinate to yield the pyridine–DPP core, followed by its alkylation employing 2-ethylhexyl bromide under basic conditions. Subsequently, a double Suzuki–Miyaura cross-coupling reaction between the alkylated dibromo pyridine–DPP derivative and the corresponding thiophene boronic ester afforded the desired thiophene capped pyridine–DPP compounds, bearing a hexyl chain at positions 3 (**3-TDPPPy**), 4 (**4-TDPPPy**), and 5 (**5-TDPPPy**) of the thiophene ring. Additionally, the derivative without hexyl substituent attached to the peripheral thiophene rings (**H-TDPPPy**) was synthesized to assess the effect of the presence of aliphatic chains on the optoelectronic properties. The structure and purity of all the compounds were confirmed by ^{1}H-NMR and ^{13}C-NMR spectroscopy (Figures S1–S4, Supporting Information) and matrix-assisted laser desorption/ionization time-of-flight (MALDI-TOF) mass spectrometry.

The thermal properties of the TDPPPy derivatives were characterized by differential scanning calorimetry (DSC) measurements (Figure S5, Supporting Information). In the second heating run, sharp endothermic peaks corresponding to the melting process were observed. Due to the presence of the hexyl side chains in the peripheral thiophenes, **3-TDPPPy** ($T_m = 119\,°C$), **4-TDPPPy** ($T_m = 148\,°C$), and **5-TDPPPy** ($T_m = 110\,°C$) displayed lower melting temperatures than **H-TDPPPy** ($T_m = 197\,°C$). Additionally, a cold crystallization appeared in the heating scan of **3-TDPPPy** ($T_{cc} = 41\,°C$) and a glass transition at ≈37 °C for **4-TDPPPy**. Besides, weaker transitions occurred for **5-TDPPPy** likely due to the formation of different mesophases which have already been observed in other DPP derivatives.[10] The cooling scan featured distinct exothermic peaks corresponding to the crystallization process for **H-TDPPPy** ($T_c = 132\,°C$), **4-TDPPPy** ($T_c = 106\,°C$), and **5-TDPPPy** ($T_c = 68\,°C$). In contrast, a broad crystallization peak was observed for **3-TDPPPy** which might indicate a lower crystallinity and explain the presence of the cold crystallization peak which results from the crystallization of the amorphous domains on heating.

2.2. Electrochemical Properties

The electrochemical properties of the four TDPPPy molecules were evaluated by cyclic voltammetry in dry dichloromethane
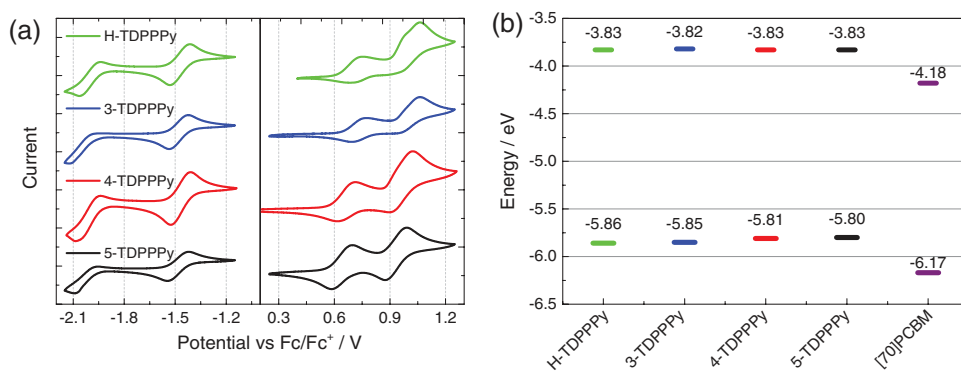
**ADVANCED
SCIENCE NEWS**
www.advancedsciencenews.com

**ADVANCED
FUNCTIONAL
MATERIALS**
www.afm-journal.de

FULL PAPER

Figure 1. a) Cyclic voltammograms of TDPPPy derivatives in 10^{-3} M CH_2Cl_2 solution containing 0.1 M tetrabutylammonium hexafluorophosphate (TBAPF$_6$) as supporting electrolyte. b) Energy levels determined by cyclic voltammetry, including those of phenyl-C$_{71}$-butyric acid methyl ester ([70]PCBM) for comparison.

solution under inert atmosphere (**Figure 1**a). The corresponding redox potentials are summarized in **Table 1**. All four compounds show two quasireversible oxidation and reduction waves. The highest occupied molecular orbital (HOMO) and lowest unoccupied molecular orbital (LUMO) energy levels were estimated from the onset of the first oxidation and reduction waves, respectively (Table 1 and Figure 1b).[11] The presence of a hexyl chain or its specific position on the peripheral thiophene has no remarkable influence on the redox potentials and hence the four TDPPPy derivatives possess virtually identical HOMO and LUMO energies. The relatively low-lying HOMO energies are due to the synergistic electron-withdrawing character of the DPP core and the pyridine moieties. The low HOMO level is expected to give a high open-circuit voltage in photovoltaic devices.

2.3. Photophyiscal Properties of TDPPPy in Solution and Film

The optical properties of the thiophene capped pyridine–DPP derivatives were determined by measuring the absorption and fluorescence spectra in dichloromethane solution and as spin-coated thin films (**Figure 2**). The spectral characteristics are summarized in Table 1. The absorption spectra of the four molecules in solution are virtually identical. The spectra represent the optical transitions among the π and π^* orbitals of the conjugated backbone. The more intense and lowest-energy absorption bands (450–620 nm) are assigned to π–π^* transitions with intramolecular charge transfer character between the electron-rich and electron-deficient moieties, while the weaker high energy

bands (300–450 nm) are ascribed to localized electronic transitions of the aromatic rings. The main absorption of **3-TDPPPy** is hypsochromically shifted relative to the other derivatives, presumably due to a slightly reduced π-conjugation as a result of a non-coplanar conformation of the thiophene and pyridine rings caused by steric hindrance between the hexyl chain pointing toward the center of the molecule and the pyridine ring (Table 1).

The absorption spectra of all four compounds shift bathochromically when going from solution to thin films on quartz substrates. This shift is a consequence of the intermolecular interactions that occur in the solid state and the increased molecular order. The shift is accompanied by the appearance of more-resolved vibronic structure and an enhanced relative intensity of the localized π–π^* absorption bands. The optical band gaps (E_g) in the solid state are in the range of 1.86–1.94 eV, as determined from the onsets of the absorption at low energy. There is a generally good correlation between the optical and the electrochemical gaps (Table 1), with slightly higher values estimated for the electrochemical gaps. This could be related to the exciton binding energy which lowers the optical gap relative to the HOMO–LUMO difference,[12] the exchange energy, and the difference in solvation energy for ions in solution compared to the neutral molecules.

The differences observed in the intensity ratio of the first two vibronic peaks, commonly referred to as the 0–0 and 0–1 transitions, in the absorption spectra allow the identification of two different types of aggregates, when the strength of the intermolecular (excitonic) coupling is similar to the electron-vibrational (vibronic) coupling. In such cases, the well-known

Table 1. Optoelectronic properties.

	$E^{ox}_{1/2}$ [a)] [V]	$E^{red}_{1/2}$ [a)] [V]	$E_g^{CVb)}$ [eV]	E_{HOMO} [c)] [eV]	E_{LUMO} [d)] [eV]	$\lambda_{max}^{abs,sol}$ [nm]	$\lambda_{max}^{abs,film}$ [nm]	ε_{sol} [e)] [M^{-1} cm^{-1}]	$E_g^{opt,filmf)}$ [eV]
H-TDPPPy	0.73, 0.98	−1.47, −2.00	2.03	−5.86	−3.83	560	593	39 700	1.94
3-TDPPPy	0.73, 1.00	−1.48, −2.05	2.03	−5.85	−3.82	549	597	31 600	1.90
4-TDPPPy	0.66, 0.96	−1.47, −2.01	1.98	−5.81	−3.83	563	622	41 600	1.87
5-TDPPPy	0.64, 0.93	−1.48, −2.03	1.97	−5.80	−3.83	566	613	43 800	1.86

[a)]$E_{1/2}$ = ½(E_{pa} + E_{pc}); [b)]Estimated as the difference between the onsets of the oxidation and reduction waves in the cyclic voltammogram; [c)]E_{HOMO} = −(5.23 + E^{ox}_{onset}); [d)]E_{LUMO} = −(5.23 + E^{red}_{onset}); [e)]Calculated from the slope of the absorbance versus concentration calibration plot using five dichloromethane solutions of different concentrations; [f)]Estimated from the onset of the lower energy band of the absorption spectrum E_g [eV] = 1240/λ_{onset} [nm].

ADVANCED
FUNCTIONAL
MATERIALS
www.afm-journal.de

ADVANCED
SCIENCE NEWS
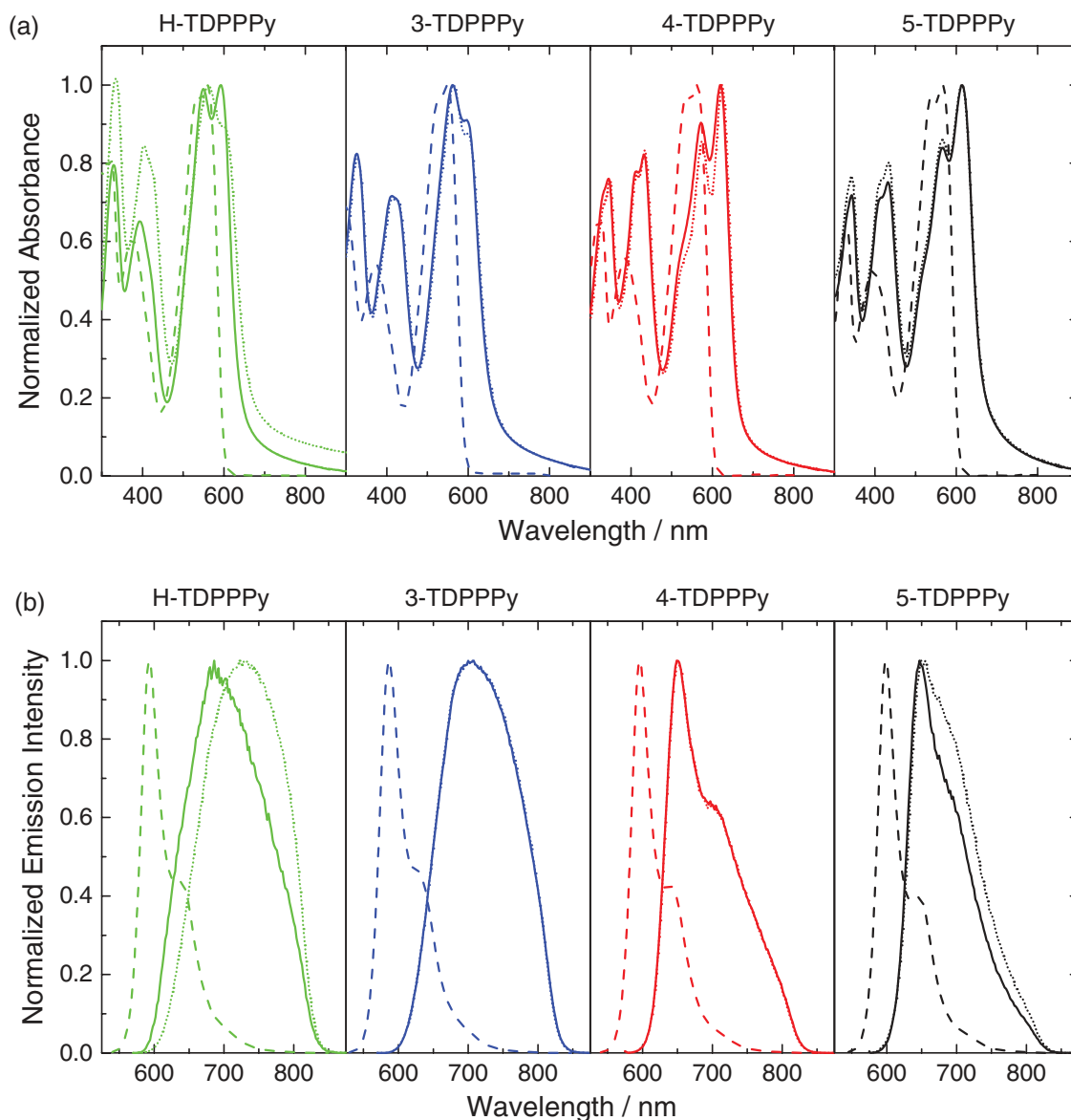www.advancedsciencenews.com

FULL PAPER

Figure 2. a) Normalized absorption and b) fluorescence spectra for the TDPPPy derivatives in dichloromethane solution (dashed line), as-cast thin films (continuous line), and after solvent vapor annealing treatment of the thin films (dotted line) on quartz substrates.

result from Kasha's theory that H-aggregates exhibit blue-shifted absorption spectra while J-aggregates exhibit the red-shifted absorption has to be modified.[13] Spano has shown that under these conditions, the two aggregate types can be distinguished by the fact that in H(J)-aggregates the ratio of the first two vibronic peak intensities in the absorption spectrum decreases (increases) with increasing excitonic coupling.[14] As can be seen in Figure 2, the 0–0/0–1 vibronic peak ratio for **3-TDPPPy** is smaller than unity, consistent with a predominant contribution of H-aggregates. In contrast, compounds **4-TDPPPy** and **5-TDPPPy** form J-type aggregates, given the 0–0/0–1 intensity ratios larger than unity. A slightly different behavior is seen for **H-TDPPPy** where the intensities of the 0–0 and 0–1 transitions are virtually the same. This is tentatively attributed to the coexistence of domains with both types of aggregates in the as-cast films.

The fluorescence spectra of the four derivatives in solution show a mirror-image relationship with the absorption spectrum, but with a more intense high-energy emission band and a weaker vibronic shoulder at longer wavelengths (Figure 2b). The identification of H- and J-aggregates in thin films was further evidenced by the characteristic features of the fluorescence spectra and the measurement of the photoluminescence lifetimes by time-correlated single photon counting. In all cases, the emission of the films was red-shifted compared to the spectra acquired in solution. However, derivatives **H-TDPPPy** and **3-TDPPPy** exhibited a broad, structureless emission band, while **4-TDPPPy** and **5-TDPPPy** exhibit vibronically structured fluorescence spectra. The characteristics are in agreement with the fact that the lowest-energy emission is strongly dipole-allowed for J-type aggregation, but forbidden in H-aggregates. The assignment is further supported by the
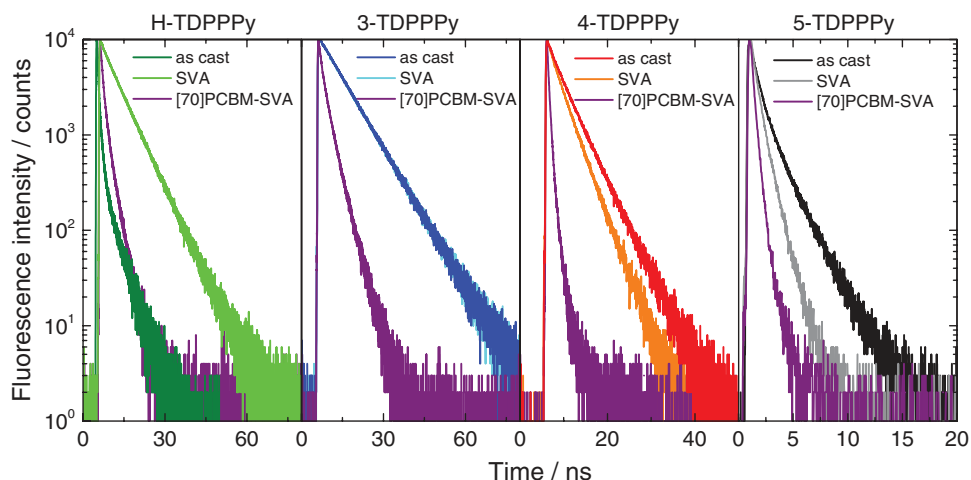
Figure 3. Time-resolved photoluminescence measurements of the thin films.

results that the fluorescence lifetimes measured for **4-TDPPPy** and **5-TDPPPy** are significantly shorter than those of **3-TDPPPy** (**Figure 3** and **Table 2**). The fluorescence decay of as-cast films of **H-TDPPPy** could only be fitted with biexponential decay, but gave a short average lifetime. The broad, structureless emission spectra of **H-TDPPPy** and **3-TDPPPy** can be explained by the fact that in a coplanar (H-type) stacking of the molecules, the resonance interaction between the molecules can result in excimer formation and hence unstructured fluorescence.

As we will show below, solvent vapor annealing (SVA) has a strong, positive effect on the performance of these materials as donors in bulk-heterojunction solar cells. Therefore, we also analyzed their photophysical characteristics after the exposure of the films to solvent vapor. The spectroscopic features of **3-TDPPPy**, **4-TDPPPy**, and **5-TDPPPy** did not change significantly after the SVA treatment; however, for **H-TDPPPy**, a pronounced solvent-vapor-induced molecular rearrangement was detected in both the absorption and the emission spectra.

The remarkable decrease of the 0–0/0–1 vibronic peak ratio in the absorption spectrum (Figure 2a), the shift to longer wavelengths of the fluorescence spectrum (Figure 2b), and the longer fluorescence lifetime (Figure 3 and Table 2) compared to the nonannealed film are all signatures of a larger contribution of the H-aggregates induced by the SVA in the solid thin films.

Summarizing, after SVA, the four molecules fall into two classes: **4-TDPPP** and **5-TDPPPy** form J-type aggregates, while **3-TDPPPy** and **H-TDPPPy** form H-type aggregates. This demonstrates that the molecular arrangement in the solid state can be significantly affected by small changes in the chemical structure, as well as by the post-treatment of the deposited thin films.

Near steady-state photoinduced absorption (PIA) measurements were performed to evaluate the nature of long-lived excited states in TDPPPy derivatives in solution. Direct excitation of TDPPPy in toluene gave no clearly detectable PIA, indicating a low quantum yield for intersystem crossing, consistent with previous results on DPP small molecules.[15] Therefore,

Table 2. Time-resolved photoluminescence parameters of the films.

Sample	Treatment	A_1	τ_1 [ns]	A_2	τ_2 [ns]	τ_{ave}[a] [ns]	k_{CT}[b] [ns^{-1}]
H-TDPPPy	n/a	4.2×10^3	0.71	4.9×10^2	4.25	2.18	–
H-TDPPPy	SVA	9.6×10^3	6.71	–	–	–	–
H-TDPPPy–[70]PCBM	SVA	8.0×10^3	0.92	2.4×10^3	2.79	1.81	0.40
3-TDPPPy	n/a	9.9×10^3	8.84	–	–	–	–
3-TDPPPy	SVA	10.2×10^3	8.23	–	–	–	–
3-TDPPPy–[70]PCBM	SVA	5.2×10^3	1.34	4.6×10^3	3.52	2.86	0.23
4-TDPPPy	n/a	9.3×10^3	4.12	–	–	–	–
4-TDPPPy	SVA	9.4×10^3	3.21	–	–	–	–
4-TDPPPy–[70]PCBM	SVA	9.6×10^3	0.42	9.0×10^2	1.22	0.59	1.38
5-TDPPPy	n/a	7.2×10^3	0.59	2.7×10^3	1.83	1.26	–
5-TDPPPy	SVA	8.3×10^3	0.48	2.7×10^3	0.98	0.68	–
5-TDPPPy–[70]PCBM	SVA	11.8×10^3	0.37	2.9×10^2	1.47	0.47	0.66

[a] $\tau_{ave} = \sum A_i \tau_i^2 / \sum A_i \tau_i$; [b] $k_{CT} = \tau_{ave,blend}^{-1} - \tau_{ave,pure}^{-1}$.
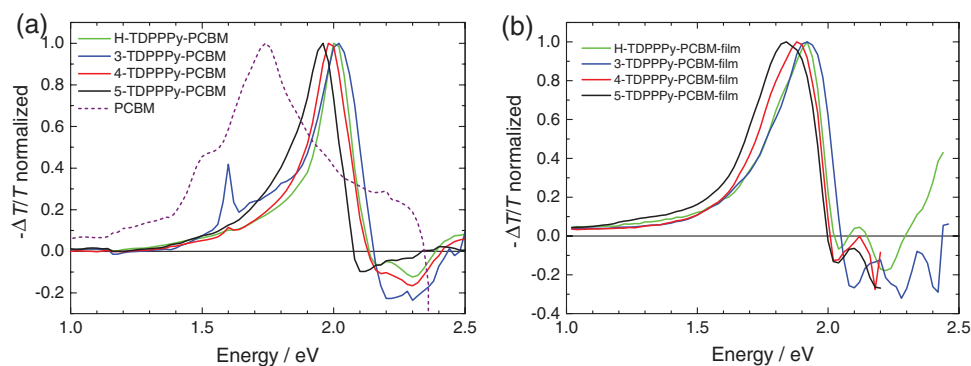
Figure 4. Normalized near steady-state PIA spectra in a) toluene solution of TDPPPy (10^{-4} M) sensitized with [60]PCBM (4×10^{-4} M), recorded at room temperature, $\lambda_{exc.} = 364$ nm, and b) spin-coated thin TDPPPy:[60]PCBM (1:4 w/w) films, recorded at 77 K, $\lambda_{exc.} = 496$ nm.

phenyl-C_{61}-butyric acid methyl ester ([60]PCBM) was employed as a triplet sensitizer given its efficient intersystem crossing from the singlet excited state to the triplet state ($E(T_1) = 1.5$ eV) with almost unit quantum yield. Codissolved with [60]PCBM, the triplet states of the TDPPPys can be populated by triplet energy transfer. The low relative permittivity of toluene ($\varepsilon_r = 2.38$) excludes charge transfer between [60]PCBM and the TDPPPys. The PIA spectra of the TDPPPy–[60]PCBM mixtures in toluene (**Figure 4**a), recorded with exciting at 364 nm, show PIA bands corresponding to the $T_n \leftarrow T_1$ absorption of the TDPPPy derivatives between 1.5 and 2.0 eV and a ground state bleaching band in the 2.1–2.5 eV range. The peak position of the $T_n \leftarrow T_1$ band (1.96–2.01 eV) follows the same trend as in the absorption and fluorescence spectra (Figure 2). The absence of the characteristic features of the triplet absorption from [60]PCBM (a shoulder $\approx$1.52 eV and a maximum $\approx$1.74 eV) in the mixed solutions evidence the successful population of the TDPPPy triplet states via energy transfer from triplet [60]PCBM.

Recent studies have reported that DPP derivatives can undergo singlet exciton fission ($S_1 + S_0 \rightarrow 2T_1$) since they fulfill the condition $E(S_1) \geq 2E(T_1)$.[16] To assess the potential of the TDPPPy derivatives in singlet fission, we assessed their triplet energies by using different quenchers with known triplet energies, such as rubrene ($E(T_1) = 1.14$ eV)[17] and bis(trihexylsiloxy) silicon-2,3-naphthalocyanine (SiNc, $E(T_1) = 0.93$ eV).[18] When rubrene was added to the TDPPPy–[60]PCBM solutions in toluene, the $T_n \leftarrow T_1$ bands of the TDPPPy derivatives remained unchanged, but adding SiNc resulted in a complete quenching of these spectral features and the appearance of a characteristic ground-state bleaching band of SiNc at 1.58 eV and a $T_n \leftarrow T_1$ absorption of SiNc at 2.10 eV (Figure S6, Supporting Information). These experiments reveal that the energy of the triplet excited states of the TDPPPy compounds in solution are in between 0.93 and 1.14 eV. This is indeed approximately half of the energy of the singlet excited state (2.07–2.12 eV) as determined from the 0–0 fluorescence peak in solution (Figure 2b) and thus satisfies the energetic requirement for singlet fission. We note that singlet fission in solution is unlikely, as it requires the close proximity of two TDPPPy molecules, of which one is the S_1 state.

PIA spectroscopy on pure TDPPPy films, recorded with excitation at 496 nm at 77 K, resulted in very low signals at photon energies of $\approx$1.8 eV. In combination with the observed fluorescence

from pure TDPPPy films, the absence of a distinct $T_n \leftarrow T_1$ signal implies that there is no evidence for the occurrence of singlet fission. Wasielewski and co-workers showed that singlet fission DPP molecules is highly dependent on the intermolecular orientation, despite favorable energetics.[16]

2.4. Photovoltaic Properties

Solution-processed bulk-heterojunction organic solar cells based on the TDPPPy derivatives as donor and phenyl-C_{71}-butyric acid methyl ester ([70]PCBM) as electron acceptor were fabricated on glass substrates with an indium tin oxide (ITO)/ MoO_3/TDPPPy–[70]PCBM/LiF/Al device configuration. The photoactive layers were spin-coated from chloroform solution with 2:1 donor:acceptor weight ratio. The use of different donor:acceptor ratios, [60]PCBM, cosolvents, or thermal treatment after the active layer deposition did not improve the performance. However, solvent vapor annealing of the blends with CS_2 vapor led to a considerable increase of the device performance, which we ascribe to an improved blend morphology.[19] The J–V characteristics of the optimized devices are presented in **Figure 5** and the photovoltaic parameters are summarized in **Table 3**.

As-cast blends without SVA exhibited low short-circuit current densities (J_{sc}), fill factors (FF), and conversion efficiencies (PCE), but a relatively high open-circuit voltage (V_{oc}) ranging from 0.81 V for **3-TDPPPy** to 0.99 V for **4-TDPPPy**, consistent with the low-lying HOMO energy levels. We note that the variation in V_{oc} ($\approx$0.2 V) is much larger than the variation in HOMO energies ($\approx$0.05 eV) determined from cyclic voltammetry. The PCE was significantly improved after the exposure of the active layers to CS_2 vapor (Table 3). SVA causes a near doubling of J_{sc}, a slight decrease in V_{oc}, and for the best devices, an enhanced FF for the blends with **4-TDPPPy** and **5-TDPPPy**. The low FF values obtained for blends based on **H-TDPPPy** and **3-TDPPPy**, even after SVA, are related to the S-shaped J–V curves around the V_{oc}.

The origin of S-shaped J–V characteristics in organic solar cells is most commonly attributed to the presence of imperfect contacts, e.g., leading to barriers at the electrodes.[20] However, also an imbalance between the electron/hole mobilities can cause an S-shape in the J–V curve.[21] As we will show below,

ADVANCED
SCIENCE NEWS
www.advancedsciencenews.com

ADVANCED
FUNCTIONAL
MATERIALS
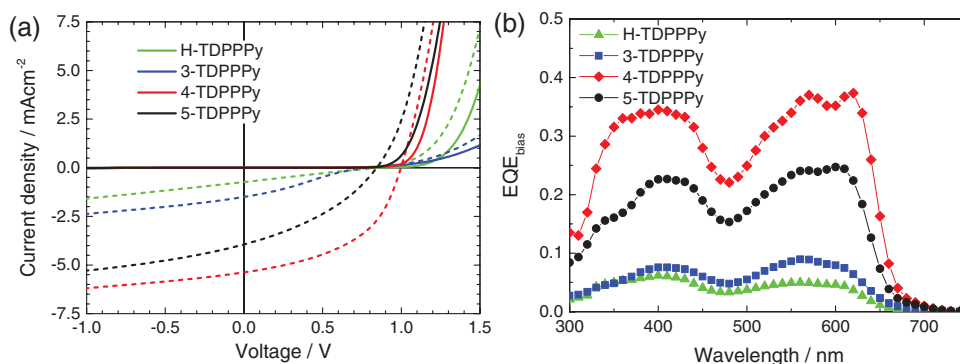www.afm-journal.de

FULL PAPER

Figure 5. a) Current density–voltage (J–V) characteristics in the dark (continuous trace) and under illumination (dashed trace). b) External quantum efficiency (EQE) spectra. All graphs correspond to devices characterized after the solvent vapor treatment.

the TDPPPys exhibit very low but almost equal hole mobilities, which cannot consistently explain the presences and absences of S-shapes in Figure 5a. On the other hand, the two molecules that do exhibit an S-shaped J–V curve, **H-TDPPPy** and **3-TDPPPy**, have slightly deeper HOMO levels than **4-TDPPPy** and **5-TDPPPy** (Table 1 and Figure 1). Based on these considerations, we tentatively attribute the S-shape for these blends to an injection barrier at the electrode. As can be seen in Figure 5a, current injection requires a substantially higher bias for **H-TDPPPy** and **3-TDPPPy** compared to **4-TDPPPy** and **5-TDPPPy**. Apart from a deeper HOMO level, the difference may also be related to the morphology of the films or the orientation of the molecules at the contacts. We note that we applied UV illumination, prior to device characterization, to enhance the Ohmicity of the contacts in all cases.

After SVA, the external quantum efficiency (EQE) value was increased from about 19% to 37% at 620 nm for **4-TDPPPy** and from 13% to 25% for **5-TDPPPy** (cf. Figure 5b and Figure S7 (Supporting Information)). In each case, the EQE essentially follows the absorption spectrum of the donor material. In particular, the EQE of **4-TDPPPy** and **5-TDPPPy** have a maximum at the first vibronic peak at 620 and 610 nm, respectively, while **H-TDPPPy** and **3-TDPPPy** have a maximum EQE at the second vibronic peak at 560 nm, consistent with their respective J- and H-aggregates. The contribution of [70]PCBM to the EQE of the cells is small, as evidenced by comparing the EQE spectra

of blends with [60]PCBM to those of [70]PCBM (cf. Figure 5b and Figure S8 (Supporting Information)). This corresponds with our recent observation that for DPP polymers mixed with PCBM, the contribution of absorption by the fullerene is generally less than that of the donor.[6]

Since the charge transport is an important parameter that influences the photovoltaic behavior, hole-only devices were fabricated to determine the hole mobility of the blends in a device configuration that corresponds to the solar cell. The hole mobilities, determined by fitting the J–V data to a space charge limited current model, were low ($\approx 10^{-7}$ cm^2 V^{-1} s^{-1} at an electric field of 10^5 V cm^{-1}) and did not vary substantially between the different blends (Figure S9 and Table S1, Supporting Information).[22] Accordingly, the different photovoltaic behavior of the four TDPPPy derivatives cannot directly be related to different hole transport properties. However, the inherent low hole mobilities can lead to an inefficient hole extraction which may limit the FF.[23]

To further determine the loss mechanisms, the EQE of the solar cells were measured with light bias of increasing intensity (see the Experimental Section for details). These measurements with increasing photon flux (Φ) allow to quantify bimolecular recombination losses. **Figure 6** shows a semilogarithmic plot of $EQE(\Phi)/EQE(\Phi_0)$, in which Φ_0 is the lowest photon flux used in the experiment, as a function of Φ with illumination at 530 nm. With increasing Φ, a manifest roll-off of this normalized EQE over the entire light intensity range is observed, which is more severe going from **4-TDPPPy**, via **5-TDPPPy** to **3-TDPPPy**. For **H-TDPPPy**, a meaningful measurement was not feasible due to the low absolute EQE at low photon fluxes. The bimolecular recombination loss efficiency, η_{BR}, can be estimated from the data using the expression: $\eta_{BR} = 1 - EQE(\Phi)/EQE(\Phi_0)$, based on the assumption that bimolecular recombination is negligible at the lowest light intensities.[24] Using this approach, we find that at short circuit, η_{BR} increases from 11% for **4-TDPPPy**, to 25% for **5-TDPPPy**, and further to 42% for **3-TDPPPy** at the highest incident light intensity. This is an interesting result considering that the only difference between the donor molecules is the position of the aliphatic chains. Apparently, minor changes in the donor molecular structure, such as the position of a side chain, can give rise to considerable variations in the device performance. We note that this analysis does not take into account possible space charge effects on the photocurrent. These may

Table 3. Photovoltaic parameters of the bulk-heterojunction solar cells.

Donor	Treatment	J_{sc}[b] [mA cm^{-2}]	V_{oc} [V]	FF	PCE[b] [%]
TDPPPy	n/a	0.11	0.90	0.24	0.02
TDPPPy	SVA[a]	0.74	0.85	0.24	0.14
3-TDPPPy	n/a	0.57	0.81	0.31	0.14
3-TDPPPy	SVA[a]	1.16	0.79	0.26	0.23
4-TDPPPy	n/a	2.72	0.99	0.31	0.83
4-TDPPPy	SVA[a]	5.40	1.00	0.48	2.60
5-TDPPPy	n/a	1.87	0.92	0.28	0.48
5-TDPPPy	SVA[a]	3.49	0.84	0.36	1.05

[a]The active layers were exposed to CS$_2$ vapor for 20 s in a Petri dish saturated with 1 mL of CS$_2$ for 60 s; [b]Calculated by integration of the EQE spectrum.

**ADVANCED
FUNCTIONAL
MATERIALS**

www.afm-journal.de

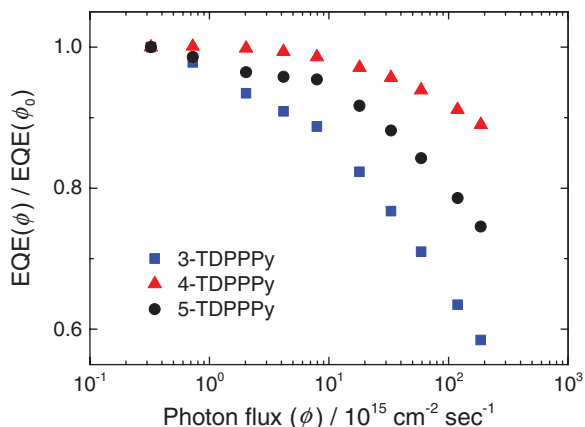**ADVANCED
SCIENCE NEWS**

www.advancedsciencenews.com

FULL PAPER

Figure 6. Photon flux dependence of EQE(Φ)/EQE(Φ_0) for three TDPPPy–[70]PCBM blends after SVA, measured with 530 nm light.

become apparent when EQE(Φ)/EQE(Φ_0) does not converge slowly to unity when $\Phi \rightarrow 0$. As can be a seen in Figure 6, this seems to be the case for **3-TDPPPy** and **5-TDPPPy**.

2.5. Morphology of TDPPPy–[70]PCBM Blends

The photovoltaic performance is generally strongly related to the morphology of the blend films. Atomic force microscopy (AFM) images of the top surfaces reveal that the blends of **4-TDPPPy** (**Figure 7**c,g) and **5-TDPPPy** (Figure 7d,g) with [70]PCBM have a lower surface roughness with smaller domain sizes than those of **H-TDPPPy** (Figure 7a,e) and **3-TDPPPy** (Figure 7b,f). This suggests that they form a more homogeneously distributed morphology when mixed with [70]PCBM, which provides enhanced exciton dissociation. The rougher surface topology for the blends of **H-TDPPPy** and **3-TDPPPy** with [70]PCBM suggests that the domain sizes of the phase

separation are larger. The size of the domains is not necessarily related to their composition and these may represent (partially) mixed domains. The root-mean-squared roughness of the blended films slightly increased upon the solvent vapor annealing treatment, suggesting that domains become larger. We note that AFM only probes the surface of the blend and that the bulk of the blend may be different, such that these results must be used with caution.

2.6. Photophysical Properties of TDPPPy–[70]PCBM Blends

To gain a deeper insight into the efficiency of the charge transfer processes and its correlation with the photovoltaic performance, time-resolved photoluminescence of the donor–acceptor blends was measured. Excitons photogenerated within the donor domains with a size smaller than the exciton diffusion length can reach the donor–acceptor interface and will be quenched when producing charges. Hence, longer lifetimes of the pristine donor materials are beneficial for the exciton migration toward donor–acceptor interface, provided that the diffusion constant is the same. Figure 3 and Table 2 show that in the pure SVA films, the H-aggregates **H-TDPPPy** and **3-TDPPPy** have distinct longer lifetimes than the J-aggregates **4-TDPPPy** and **5-TDPPPy**. On the other hand, exciton diffusion in H-aggregates is generally slower than in J-aggregates,[25] such that a beneficial longer lifetime would be compensated by a detrimental slower diffusion. We find that for each of the TDPPPy–[70]PCBM blends, the photoluminescence lifetime is considerably shorter than in the pure donor material, indicating effective exciton quenching. The fluorescence decay of the donor–acceptor blends (Figure 3) can be well fitted to a biexponential decay with a fast component (τ_1) and a slow component (τ_2). The short lifetime is ascribed to donor molecules that are in close proximity to [70]PCBM in the blend to transfer an electron, while the long lifetime likely originates from relative pure
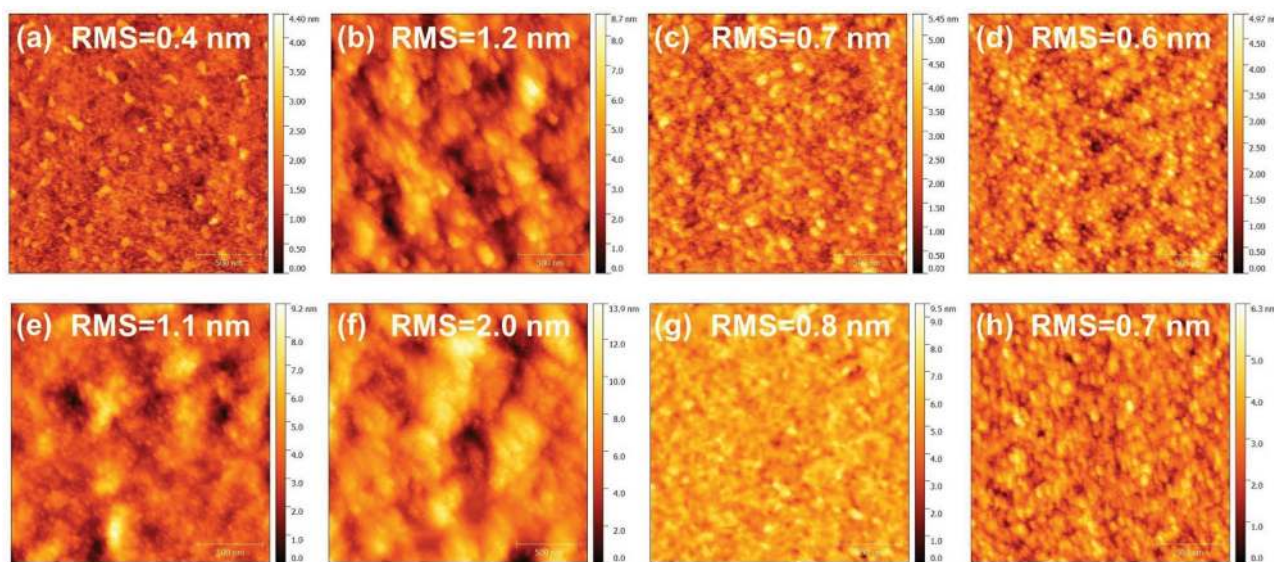

Figure 7. Tapping-mode AFM height images of the active layers a–d) without and e–h) after SVA. (a, e) **H-TDPPPy**, (b, f) **3-TDPPPy**, (c, g) **4-TDPPPy**, (d, h) **5-TDPPPy**. Scan size: 2 μm × 2 μm.

ADVANCED
SCIENCE NEWS
www.advancedsciencenews.com

ADVANCED
FUNCTIONAL
MATERIALS
www.afm-journal.de

FULL PAPER
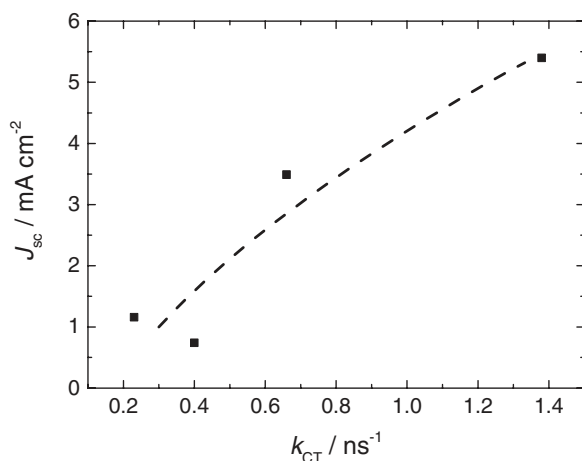
Figure 8. Plot of J_{sc} versus k_{CT} for the four TDPPPy–[70]PCBM blends. The line is a guide to the eye.

Figure 9. Schematic representation of the singlet (S_1) and triplet (T_1) excited states relative to the ground state (S_0) of the TDPPPy donors, PCBM, and the charge transfer (CT) state showing the possible energy (dashed arrows) and charge (solid arrows) transfer processes and optical transitions observed in (photoinduced) absorption spectroscopy (grey arrows).

donor domains in the blend that do not strongly contribute to charge generation.[26] Consistent with the presence of H- and J-aggregates, the blends of **H-TDPPPy** and **3-TDPPPy** displayed longer slow decay components (2.79 and 3.52 ns, respectively) than **4-TDPPPy** and **5-TDPPPy** (1.22 and 1.47 ns), respectively. By comparing the (average) lifetimes in the blend and in the pure donor, it is possible to extract an average charge transfer rate k_{CT}.[27] This rate is slower for **H-TDPPPy** and **3-TDPPPy** (0.40 and 0.23 ns^{-1}, respectively) than for **4-TDPPPy** and **5-TDPPPy** (1.38 and 0.66 ns^{-1}, respectively). This suggests an overall more efficient charge generation process in blends of **4-TDPPPy** and **5-TDPPPy** with the [70]PCBM acceptor. **Figure 8** shows a plot of J_{sc} versus k_{CT}, which strongly suggests that in these blends, charge generation is the main parameter that determines the short-circuit current.

To investigate the nature of long-lived photoexcitations in TDPPPy–[70]PCBM blends, we used near steady-state PIA spectroscopy. The PIA spectra of TDPPPy–[60]PCBM blend films recorded under similar conditions, on the other hand, displayed much more intense PIA bands with maxima in the range of 1.84–1.92 eV (Figure 4b). Although broadened and shifted to slightly lower energies, these absorption bands are very similar to those observed for the TDPPPy triplet states in toluene solution (Figure 4a). Hence, the PIA features are assigned to the $T_n \leftarrow T_1$ absorption of TDPPPy. No signs of charges on TDPPPy or [60]PCBM are observed in the PIA. Because direct excitation of pure TDPPPy does not result in appreciable formation of T_1 states (see Section 2.3), the triplet excited states of the TDPPPy derivatives in the blends with [60]PCBM are likely populated via a charge recombination from the TDPPPy$^+$–[60]PCBM$^-$ charge transfer (CT) state. Formation of an initial charge transfer state is evident from the photocurrent (Figure 5) and supported by TDPPPy fluorescence quenching by [70]PCBM (Figure 3). Charge recombination into the triplet state is a well-established loss mechanism in donor–acceptor that occurs when the triplet state of either of the components is below that of the charge transfer state ($E(T_1) < E(CT)$).[28] The T_1 states of TDPPPy and [60]PCBM are at 0.93–1.14 and 1.50 eV, respectively. The energy of the CT state can be estimated from the V_{oc} via the empirical relation $E(CT) = qV_{oc} + 0.5$ eV,[29] to be 1.3–1.5 eV, i.e., higher
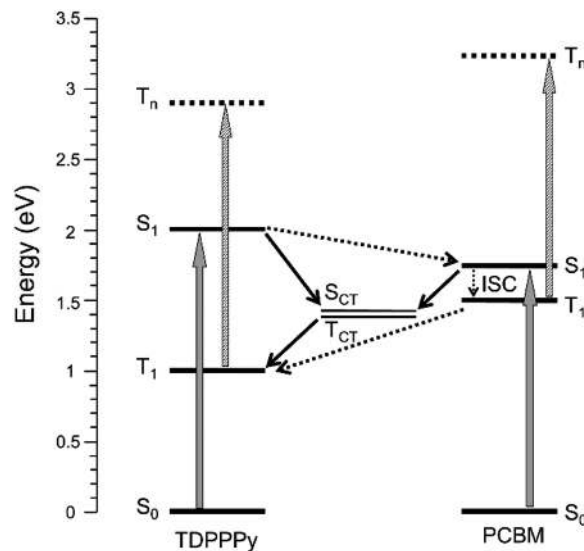
than $E(T_1)$ of TDPPPy. **Figure 9** shows these levels in a state diagram, where we assume that the splitting between the singlet and triplet CT states is small because the hole and electron are on different molecules. We note that we cannot exclude that in films, the T_1 of TDPPPy is formed via a sequence of two energy transfer steps mediated by intersystem crossing of [60]PCBM:TDPPPy(S_1) → [60]PCBM(S_1) → [60]PCBM(T_1) → TDPPPy(T_1). Such mechanism has been shown to occur in covalently linked oligomer–fullerene systems in solution.[30]

To investigate if the triplet state energy of TDPPPy is different in film compared to solution, we studied the PIA of ternary blend films consisting of TDPPPy–[60]PCBM–quencher, with rubrene or SiNc as quencher. **Figure 10**a (and Figure S10 in the Supporting Information) shows that in combination with rubrene, the TDPPPy T_1 states are not quenched, except for **3-TDPPPy** where the intensity of the $T_n \leftarrow T_1$ bands is reduced. Detection of the corresponding $T_n \leftarrow T_1$ absorption of rubrene (2.48 eV) is hampered by the scattering from the excitation light (2.50 eV). The results suggest that the T_1 state of **3-TDPPPy** is almost degenerated with that of rubrene (1.14 eV). In contrast, when SiNc was used, the TDPPPy T_1 states were quenched with the concomitant observation of the characteristic spectral features of the SiNc T_1 state (Figure 10b). The PIA experiments show that the structural difference between the four TDPPPy compounds and their different arrangement in the solid films have a minor influence on the energies of the T_1 states.

3. Conclusion

Four different small-molecule diketopyrrolo[3,4-c]pyrrole derivatives flanked by pyridine moieties directly attached to the DPP core and end-capped with thiophene rings bearing aliphatic
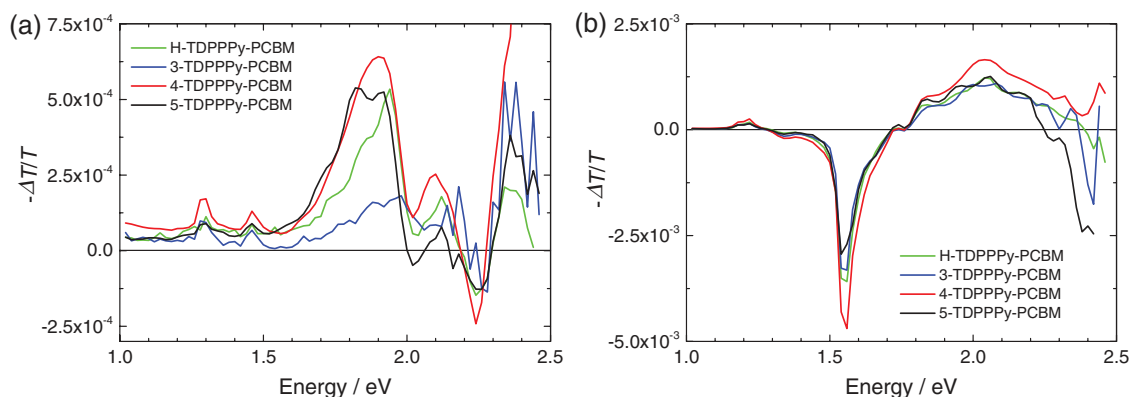
ADVANCED
FUNCTIONAL
MATERIALS
www.afm-journal.de

ADVANCED
SCIENCE NEWS
www.advancedsciencenews.com

Figure 10. Near steady-state PIA spectra of spin-coated TDPPPy–[60]PCBM–quencher (1:4:1 w/w/w) thin films recorded at 77 K, $\lambda_{exc.}$ = 496 nm with a) rubrene and b) SiNc as quencher.

chains at different positions have been synthesized and characterized. The photophysical response of these derivatives as spin-cast thin films shows that the different derivatives assemble into H-type or J-type aggregates. Without a side chain on the thiophene in **H-TDPPPy** or in the presence of a hexyl chain at the 3-position of the thiophene ring in **3-TDPPPy**, H-type aggregates are formed. For **H-TDPPPy** solvent vapor annealing efficiently transformed the as-cast film with mixed H- and J-aggregates into H-aggregates. In contrast, when the hexyl chains are at 4- or 5-positions as in **4-TDPPPy** or **5-TDPPPy**, a predominant J-type behavior is identified. Interestingly, the H-type or J-type aggregation correlates with the photovoltaic performance of the bulk-heterojunction solar cells. The molecules that form H-aggregates displayed distinctly lower performance than those forming J-aggregates. The difference is up to an order of magnitude. The best cells were obtained for **4-TDPPPy** after SVA, which showed a J_{sc}, V_{oc}, FF, and PCE of 5.40 mA cm^{-2}, 1.00 V, 0.48, and 2.60%, respectively. The higher performance of **4-TDPPPy** and **5-TDPPPy** compared to **3-TDPPPy** and **H-TDPPPy** is the result of a faster charge transfer rate and reduced bimolecular recombination. While the faster charge generation might be caused by more efficient exciton diffusion in J-aggregates, the origin of the reduced bimolecular recombination is less clear and is tentatively attributed to a more beneficial morphology. We did not observe significant difference in the macroscopic charge transport properties of these materials that could explain the different performance. In TDPPPy–[60]PCBM blends, photoexcitation ultimately produces TDPPPy triplet states as the only surviving long-lived photoexcitation, formed via charge recombination from the charge separated state.

4. Experimental Section

Reagents used as starting materials and commercial solvents were used as received without further purification. Unless stated otherwise, all reactions were performed under argon atmosphere. ^{1}H NMR and ^{13}C NMR spectra were recorded on a Varian Mercury spectrometer having frequencies of 400 MHz for proton nuclei and 100 MHz for carbon nuclei. Chemical shifts are given in ppm and were referenced to the residual peak from the deuterated solvent. MALDI-TOF mass spectroscopy was recorded on a Bruker Autoflex Speed spectrometer. DSC measurements were performed using a TA Instruments

Q2000-1037 DSC with heating and cooling rates of 10 °C min^{-1} under nitrogen. The second heating run was analyzed. Ultraviolet-visible–near-infrared (UV–vis–NIR) spectroscopy was conducted on a Perkin Elmer Lambda 1050 spectrophotometer. Emission spectra were recorded on an Edinburgh Instruments FLSP920 double-monochromator spectrophotometer. Time-resolved photoluminescence measurements were performed on an Edinburgh Instruments LifeSpec-PS spectrophotometer with excitation at 400 nm. Cyclic voltammetry was performed under an inert atmosphere using an Autolab potentiostat with a scan speed of 0.1 V s^{-1} and 0.1 M tetrabutylammonium hexafluorophosphate in dichloromethane as electrolyte. Ferrocene was used as an internal reference, a platinum disk as working electrode, a silver rod as counter-electrode, and Ag/AgCl as reference electrode.

Near steady-state photoinduced absorption spectra were recorded by excitation at 364 or 496 nm with a mechanically modulated (275 Hz) CW argon ion laser pump beam and by measuring the change in transmission of a tungsten-halogen probe beam through the sample (ΔT) with a phase-sensitive lock-in amplifier after dispersion with a monochromator and detection using Si and InGaAs detectors. The pump power was 50 or 100 mW with a beam diameter of 2 mm. The signal intensity ($-\Delta T/T$) was corrected for the photoluminescence, which was recorded in a separate experiment. Measurements in solution were carried out at room temperature. Thin film samples were held at 77 K in an inert nitrogen atmosphere using an Oxford Optistat continuous flow cryostat. Samples in solution were prepared inside a glovebox by dissolving the corresponding TDPPPy derivative (10^{-4} M) blended with [60]PCBM (4×10^{-4} M) in dry, deoxygenated toluene. Thin films were spin-coated from chloroform solution of TDPPPy (10 mg mL^{-1}) and [60]PCBM (1:4 by weight) on glass substrates. The quencher concentration for the triplet energy estimation was 10^{-4} M in solution and 10 mg mL^{-1} for the films.

For the photovoltaic device preparation, prepatterned ITO covered glass substrates (Naranjo Substrates) with an active area of 0.09 and 0.16 cm^2 were cleaned by sonication in acetone, scrubbing, and subsequent sonication with a sodium dodecyl sulfate solution, rinsing with demineralized water, and finally, sonication in isopropanol for 15 min at each step. After 30 min of UV-ozone treatment, the substrates were transferred to a glovebox for the thermal evaporation of a 10 nm thick layer of MoO$_3$ under high vacuum ($\approx$3 × 10^{-7} mbar). Subsequently, the active layer consisting of a blend of the corresponding donor and [70]PCBM (2:1 by weight) was spin-coated from a chloroform solution (10 mg mL^{-1}). Then, the solvent vapor annealing treatment was applied placing the substrates for 20 s in a Petri dish previously saturated with 1 mL of CS$_2$ for 1 min at room temperature. Finally, a 1 nm thick layer of LiF and a 100 nm thick layer of Al were thermally evaporated under high vacuum ($\approx$3 × 10^{-7} mbar) as back electrode. The active layer thicknesses ($\approx$100 nm) were measured with a Veeco Dektak 150 profilometer. Prior to the device characterization, substrates were exposed to UV illumination for 15 min. J–V characteristics were

measured with a Keithley 2400 source meter under ≈100 mW cm^{-2} white light illumination from a tungsten-halogen lamp filtered by a Schott GG385 UV filter and a Hoya LB120 daylight filter. Short-circuit currents under AM1.5G conditions were determined by integrating the spectral response with the solar spectrum. Spectral response measurements were conducted under 1 sun operating conditions by using a 530 nm high power light-emitting diode (LED) (Thorlabs) for bias illumination. The device was kept in a nitrogen filled box behind a quartz window and irradiated with modulated monochromatic light, from a 50 W tungsten-halogen lamp (Osram 64610) and monochromator (Oriel, Cornerstone 130) with the use of a mechanical chopper. The response was recorded as a voltage from a preamplifier (SR570) using a lock-in amplifier (SR830). A calibrated silicon cell was used as reference.

Light intensity measurements of the EQE were performed at 530 nm using a high power LED (Thorlabs). This allows very accurate and precise electronic control of the light intensity, which was measured separately and converted to a photon flux (Φ) using a calibrated Si photodiode. The short-circuit current (J_{sc}) of the cell is divided by Φ to obtain the EQE = J_{sc}/Φ at each photon flux Φ. The extent of bimolecular recombination can be estimated from $\eta_{BR} = 1 - \text{EQE}(\Phi)/\text{EQE}(\Phi_0)$, where Φ_0 is the lowest photon flux in the experiment. This analysis assumes that bimolecular recombination is negligible at the lowest light intensities and holds when $\text{EQE}(\Phi)/\text{EQE}(\Phi_0)$ convergences slowly to unity when $\Phi \to 0$.

For mobility evaluation, single carrier devices were fabricated with the following structure: ITO/MoO$_3$(10 nm)/active layer/MoO$_3$(10 nm)/Ag(100 nm). The hole mobilities were estimated by fitting the J–V characteristics to the Murgatroyd equation: $J = \frac{9}{8}\varepsilon_0\,\varepsilon_r\,\mu_0\,\frac{V^2}{L^3}\exp\left(0.89\beta\sqrt{\frac{V}{L}}\right)$, where J is the current density, ε_0 the permittivity of vacuum (8.85×10^{-14} F cm^{-1}), ε_r the relative permittivity of the active layer (3), μ_0 the zero-field mobility, L the thickness of the active layer, and β the field-activation factor. The voltage was corrected for the built-in voltage (V_{bi}) and the voltage drop (V_r). The charge carrier mobility was determined using the Poole–Frenkel relationship, $\mu = \mu_0\exp(\beta E^{1/2})$, at an electric field of 10^5 V cm^{-1}.

AFM measurements were performed on an extended Veeco MultiMode AFM connected to a Nanoscope III controller in tapping mode using PPP-NCH-50 probes (Nanosensors).

Supporting Information

Supporting Information is available from the Wiley Online Library or from the author.

Acknowledgements

[1] a) H. Yao, L. Ye, H. Zhang, S. Li, S. Zhang, J. Hou, *Chem. Rev.* **2016**, *116*, 7397; b) W. Ni, X. Wan, M. Li, Y. Wang, Y. Chen, *Chem. Commun.* **2015**, *51*, 4936; c) L. Lu, T. Zheng, Q. Wu, A. M. Schneider, D. Zhao, L. Yu, *Chem. Rev.* **2015**, *115*, 12666;

d) L. Dou, Y. Liu, Z. Hong, G. Li, Y. Yang, *Chem. Rev.* **2015**, *115*, 12633.

[2] a) Q. Zhang, B. Kan, F. Liu, G. Long, X. Wan, X. Chen, Y. Zuo, W. Ni, H. Zhang, M. Li, Z. Hu, F. Huang, Y. Cao, Z. Liang, M. Zhang, T. P. Russell, Y. Chen, *Nat. Photonics* **2015**, *9*, 35; b) B. Kan, M. Li, Q. Zhang, F. Liu, X. Wan, Y. Wang, W. Ni, G. Long, X. Yang, H. Feng, Y. Zuo, M. Zhang, F. Huang, Y. Cao, T. P. Russell, Y. Chen, *J. Am. Chem. Soc.* **2015**, *137*, 3886; c) B. Kan, Q. Zhang, M. Li, X. Wan, W. Ni, G. Long, Y. Wang, X. Yang, H. Feng, Y. Chen, *J. Am. Chem. Soc.* **2014**, *136*, 15529.

[3] M. Grzybowski, D. T. Gryko, *Adv. Opt. Mater.* **2015**, *3*, 280.

[4] W. Li, K. H. Hendriks, M. M. Wienk, R. A. J. Janssen, *Acc. Chem. Res.* **2016**, *49*, 78.

[5] a) J. Yue, S. Sun, J. Liang, W. Zhong, L. Lan, L. Ying, F. Huang, W. Yang, Y. Cao, *J. Mater. Chem. C* **2016**, *4*, 2470; b) A. Purc, M. Banasiewicz, E. Glodkowska-Mrowka, D. T. Gryko, *J. Mater. Chem. C* **2016**, *4*, 2877; c) C. J. Mueller, C. R. Singh, M. Thelakkat, *J. Polym. Sci., Part B: Polym. Phys.* **2016**, *54*, 639; d) C. J. Mueller, T. Klein, E. Gann, C. R. McNeill, M. Thelakkat, *Macromolecules* **2016**, *49*, 3749; e) P. Li, L. Xu, H. Shen, X. Duan, J. Zhang, Z. Wei, Z. Yi, C.-a. Di, S. Wang, *ACS Appl. Mater. Interfaces* **2016**, *8*, 8620; f) J. Kuwabara, N. Takase, T. Yasuda, T. Kanbara, *J. Polym. Sci., Part A.* **2016**, *54*, 2337; g) F. Guo, X. Liu, Y. Ding, F. Kong, W. Chen, L. Zhou, S. Dai, *RSC Adv.* **2016**, *6*, 13433; h) X. Zhang, C. Xiao, A. Zhang, F. Yang, H. Dong, Z. Wang, X. Zhan, W. Li, W. Hu, *Polym. Chem.* **2015**, *6*, 4775; i) J. Yue, J. Liang, S. Sun, W. Zhong, L. Lan, L. Ying, W. Yang, Y. Cao, *Dyes Pigm.* **2015**, *123*, 64; j) B. Sun, W. Hong, H. Aziz, Y. Li, *Polym. Chem.* **2015**, *6*, 938; k) C. J. Mueller, C. R. Singh, M. Fried, S. Huettner, M. Thelakkat, *Adv. Funct. Mater.* **2015**, *25*, 2725; l) J. W. Lee, H. Ahn, W. H. Jo, *Macromolecules* **2015**, *48*, 7836; m) B. Sun, W. Hong, Z. Yan, H. Aziz, Y. Li, *Adv. Mater.* **2014**, *26*, 2636; n) J. W. Jung, F. Liu, T. P. Russell, W. H. Jo, *Chem. Commun.* **2013**, *49*, 8495; o) C. J. Mueller, M. Brendel, P. Ruckdeschel, J. Pflaum, M. Thelakkat, *Adv. Energy Mater.* **2015**, *5*, 1500914.

[6] K. H. Hendriks, A. S. G. Wijpkema, J. J. van Franeker, M. M. Wienk, R. A. J. Janssen, *J. Am. Chem. Soc.* **2016**, *138*, 10026.

[7] a) V. S. Gevaerts, E. M. Herzig, M. Kirkus, K. H. Hendriks, M. M. Wienk, J. Perlich, P. Müller-Buschbaum, R. A. J. Janssen, *Chem. Mater.* **2014**, *26*, 916; b) Y. S. Choi, T. J. Shin, W. H. Jo, *ACS Appl. Mater. Interfaces* **2014**, *6*, 20035.

[8] a) Q. Wang, J. J. van Franeker, B. J. Bruijnaers, M. M. Wienk, R. A. J. Janssen, *J. Mater. Chem. A* **2016**, *4*, 10532; b) C. E. Song, Y. J. Kim, S. R. Suranagi, G. P. Kini, S. Park, S. K. Lee, W. S. Shin, S.-J. Moon, I.-N. Kang, C. E. Park, J.-C. Lee, *ACS Appl. Mater. Interfaces* **2016**, *8*, 12940; c) M. Jung, Y. Yoon, J. H. Park, W. Cha, A. Kim, J. Kang, S. Gautam, D. Seo, J. H. Cho, H. Kim, J. Y. Choi, K. H. Chae, K. Kwak, H. J. Son, M. J. Ko, H. Kim, D.-K. Lee, J. Y. Kim, D. H. Choi, B. Kim, *ACS Nano* **2014**, *8*, 5988; d) R. Fitzner, C. Elschner, M. Weil, C. Uhrich, C. Körner, M. Riede, K. Leo, M. Pfeiffer, E. Reinold, E. Mena-Osteritz, P. Bäuerle, *Adv. Mater.* **2012**, *24*, 675.

[9] J. Liu, Y. Zhang, H. Phan, A. Sharenko, P. Moonsin, B. Walker, V. Promarak, T.-Q. Nguyen, *Adv. Mater.* **2013**, *25*, 3645.

[10] J. Mei, K. R. Graham, R. Stalder, S. P. Tiwari, H. Cheun, J. Shim, M. Yoshio, C. Nuckolls, B. Kippelen, R. K. Castellano, J. R. Reynolds, *Chem. Mater.* **2011**, *23*, 2285.

[11] C. M. Cardona, W. Li, A. E. Kaifer, D. Stockdale, G. C. Bazan, *Adv. Mater.* **2011**, *23*, 2367.

[12] a) J.-L. Bredas, *Mater. Horiz.* **2014**, *1*, 17; b) T. Johansson, W. Mammo, M. Svensson, M. R. Andersson, O. Inganas, *J. Mater. Chem.* **2003**, *13*, 1316.

[13] M. Kasha, *Radiat. Res.* **1963**, *20*, 55.

[14] F. C. Spano, *Acc. Chem. Res.* **2010**, *43*, 429.

[15] a) B. P. Karsten, R. A. J. Janssen, *Macromol. Chem. Phys.* **2011**, *212*, 515; b) B. P. Karsten, R. K. M. Bouwer, J. C. Hummelen,

R. M. Williams, R. A. J. Janssen, *Photochem. Photobiol. Sci.* **2010**, *9*, 1055.

[16] a) P. E. Hartnett, E. A. Margulies, C. M. Mauck, S. A. Miller, Y. Wu, Y.-L. Wu, T. J. Marks, M. R. Wasielewski, *J. Phys. Chem. B* **2016**, *120*, 1357; b) C. M. Mauck, P. E. Hartnett, E. A. Margulies, L. Ma, C. E. Miller, G. C. Schatz, T. J. Marks, M. R. Wasielewski, *J. Am. Chem. Soc.* **2016**, *138*, 11749.

[17] W. G. Herkstroeter, P. B. Merkel, *J. Photochem.* **1981**, *16*, 331.

[18] P. A. Firey, W. E. Ford, J. R. Sounik, M. E. Kenney, M. A. J. Rodgers, *J. Am. Chem. Soc.* **1988**, *110*, 7626.

[19] a) J.-L. Wang, Z. Wu, J.-S. Miao, K.-K. Liu, Z.-F. Chang, R.-B. Zhang, H.-B. Wu, Y. Cao, *Chem. Mater.* **2015**, *27*, 4338; b) C. D. Wessendorf, G. L. Schulz, A. Mishra, P. Kar, I. Ata, M. Weidelener, M. Urdanpilleta, J. Hanisch, E. Mena-Osteritz, M. Lindén, E. Ahlswede, P. Bäuerle, *Adv. Energy Mater.* **2014**, *4*, 1400266; c) K. Sun, Z. Xiao, E. Hanssen, M. F. G. Klein, H. H. Dam, M. Pfaff, D. Gerthsen, W. W. H. Wong, D. J. Jones, *J. Mater. Chem. A* **2014**, *2*, 9048.

[20] a) O. J. Sandberg, M. Nyman, R. Österbacka, *Phys. Rev. Appl.* **2014**, *1*, 024003; b) W. Tress, O. Inganäs, *Sol. Energy Mater. Sol. Cells* **2013**, *117*, 599; c) W. Tress, S. Corvers, K. Leo, M. Riede, *Adv. Energy Mater.* **2013**, *3*, 873; d) A. Wagenpfahl, D. Rauh, M. Binder, C. Deibel, V. Dyakonov, *Phys. Rev. B* **2010**, *82*, 115306.

[21] W. Tress, A. Petrich, M. Hummert, M. Hein, K. Leo, M. Riede, *Appl. Phys. Lett.* **2011**, *98*, 063301.

[22] a) G. G. Malliaras, J. R. Salem, P. J. Brock, C. Scott, *Phys. Rev. B* **1998**, *58*, R13411; b) P. N. Murgatroyd, *J. Phys. D: Appl. Phys.* **1970**, *3*, 151.

[23] a) V. D. Mihailetchi, J. Wildeman, P. W. M. Blom, *Phys. Rev. Lett.* **2005**, *94*, 126602; b) C. M. Proctor, C. Kim, D. Neher, T.-Q. Nguyen, *Adv. Funct. Mater.* **2013**, *23*, 3584; c) D. Credgington, F. C. Jamieson, B. Walker, T.-Q. Nguyen, J. R. Durrant, *Adv. Mater.* **2012**, *24*, 2135.

[24] L. J. A. Koster, M. Kemerink, M. M. Wienk, K. Maturová, R. A. J. Janssen, *Adv. Mater.* **2011**, *23*, 1670.

[25] a) L. D. A. Siebbeles, A. Huijser, T. J. Savenije, *J. Mater. Chem.* **2009**, *19*, 6067; b) K. Tennakone, P. K. D. D. P. Pitigala, A. G. U. Perera, *RSC Adv.* **2013**, *3*, 2770.

[26] B. Bernardo, D. Cheyns, B. Verreet, R. D. Schaller, B. P. Rand, N. C. Giebink, *Nat. Commun.* **2014**, *5*, 3245.

[27] J. Lakowicz, *Principles of Fluorescence Spectroscopy*, Springer Science+Business Media, New York, **2006**.

[28] a) T. A. Ford, I. Avilov, D. Beljonne, N. C. Greenham, *Phys. Rev. B* **2005**, *71*, 125212; b) T. Offermans, P. A. van Hal, S. C. J. Meskers, M. M. Koetse, R. A. J. Janssen, *Phys. Rev. B* **2005**, *72*, 045213.

[29] a) K. Vandewal, A. Gadisa, W. D. Oosterbaan, S. Bertho, F. Banishoeib, I. Van Severen, L. Lutsen, T. J. Cleij, D. Vanderzande, J. V. Manca, *Adv. Funct. Mater.* **2008**, *18*, 2064; b) D. Veldman, S. C. J. Meskers, R. A. J. Janssen, *Adv. Funct. Mater.* **2009**, *19*, 1939.

[30] B. P. Karsten, P. P. Smith, A. B. Tamayo, R. A. J. Janssen, *J. Phys. Chem. A* **2012**, *116*, 1146.